*Advanced Physics Research*

ADVANCED PHYSICS RESEARCH Open Access

www.advphysicsres.com

RESEARCH ARTICLE OPEN ACCESS

# Elucidating the Effect of Ferroelectricity in Bismuth Ferrite Solar Cells

Marcel Habrik[1,2] | Susanne Wagner[1,3] | Holger Röhm[1,2] | Alexander Colsmann[1,2]

[1]Material Research Center For Energy Systems, Karlsruhe Institute of Technology, Karlsruhe, Germany | [2]Light Technology Institute, Karlsruhe Institute of Technology, Karlsruhe, Germany | [3]Ceramic Materials and Technologies, Karlsruhe Institute of Technology, Karlsruhe, Germany

**Correspondence:** Alexander Colsmann (alexander.colsmann@kit.edu)

**Received:** 25 March 2026 | **Revised:** 6 July 2026 | **Accepted:** 30 July 2026

**Keywords:** $BiFeO_3$ | ferroelectricity | photovoltaic effect | solar cell

## ABSTRACT

To investigate the photoresponse of metal-ferroelectric-metal (MFM) devices, we sandwich polycrystalline bismuth ferrite between two electrodes of similar work function. We use calcium-substitution on the A-site to tailor the properties of bismuth ferrite $Bi_{1-x}Ca_xFeO_{3-\delta}$ from ferroelectric ($x < 0.2$) to nonferroelectric ($x > 0.2$). Devices with nonferroelectric $Bi_{1-x}Ca_xFeO_{3-\delta}$ show symmetric current density-voltage ($J$–$V$) curves and no photoresponse, resembling their symmetric electronic properties that originate from two opposing Schottky junctions at the symmetric electrodes. In contrast, the $J$–$V$ curves of ferroelectric $Bi_{1-x}Ca_xFeO_{3-\delta}$ are governed by the polarization direction, introducing directionality through modification of the Schottky barriers. Under illumination, the polarization induced modulation of the Schottky barriers promotes directionality of the photogenerated charge carriers and leverages enhanced photocurrents.

## 1 | Introduction

After more than a decade of flourishing research on perovskite solar cells, the field started to target less toxic and more long-term stable compounds with similar properties, examples of which include halides, sulfites and oxides [1–3]. In particular oxides appear an interesting class of materials when the research is guided by long-term stability. Many of the semiconducting oxides with perovskite structure are of ferroelectric nature which may or may not govern their optoelectronic properties, in particular charge carrier separation and collection at the electrodes [3, 4].

Various studies in the literature have explored the photocurrent and the photovoltaic effect of ferroelectric thin-film devices with metal/ferroelectric/metal (MFM) architectures [3, 5–7]. Typical photocurrent densities range from nA $cm^{-2}$ to µA $cm^{-2}$, which is largely attributed to low charge carrier mobilities and low charge carrier densities in ferroelectric oxides [7–9]. Different theoretic models have been proposed to explain charge carrier separation and the origin of current directionality in MFM devices. In single crystal oxides, the bulk-photovoltaic effect, the domain wall conduction model, and the depolarization field model are often discussed [10–15]. In semiconducting polycrystalline MFM devices, an extended Schottky barrier model prevails, where the difference between the work function of the metal and the electrochemical potential of the ferroelectric induces space charges at the interface [8, 16–18].

In this work, we investigate the modulation of ferroelectric/metal interfaces upon ferroelectric poling and their influence on the photovoltaic properties of MFM devices. For this purpose, we utilize polycrystalline, ferroelectric bismuth ferrite ($BiFeO_3$) sandwiched between a fluorine-doped tin oxide (FTO) and a silver electrode. $BiFeO_3$ exhibits a large polarization at room temperature ($2Pr = 110$ µC $cm^{-2}$) [19] and semiconducting properties (band gap $E_g = 2.7$ eV) [20–22]. Partial substitution

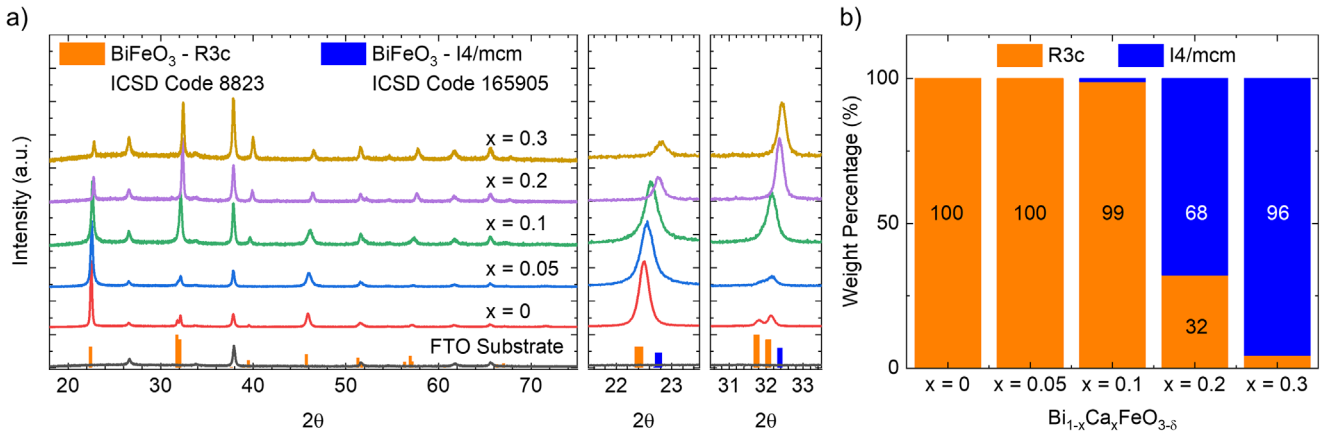


**FIGURE 1** | (a) XRD pattern of $Bi_{1-x}Ca_xFeO_{3-\delta}$ thin films (x = 0, 0.05, 0.1, 0.2, 0.3) grown on FTO-coated glass substrates, recorded at room temperature. The right panel shows details of the XRD peaks at $2\theta = 22.4°$ (012), 31.7° (104) and 32° (110). For reference, the peak positions of the rhombohedral $BiFeO_3$ crystal phase (R3c, ICSD 8823) are indicated in orange and the peak positions of the tetragonal crystal phase (I4/mcm, ICSD 165905) are indicated in blue. (b) Weight percentage of R3c and I4/mcm phases in dependence of the amount of calcium inclusion.

of bismuth with calcium changes the ferroelectric R3c phase of $BiFeO_3$ to the nonferroelectric I4/mcm phase which allows us the direct comparison of the interfaces of ferroelectric and nonferroelectric $BiFeO_3$ with the electrodes.

## 2 | Crystal Structure

Elemental substitution is often employed to tailor the optical, electrical or ferroic properties of oxide perovskites. In this work, $BiFeO_3$ thin films are modified by partial substitution of bismuth with calcium on the A-site to tailor the strength of the ferroelectric polarization from ferroelectric to non-ferroelectric. To this end, we deposited the $BiFeO_3$ thin films from a solute of bismuth(III) nitrate pentahydrate ($Bi(NO_3)_3{\cdot}5\,H_2O$) and iron(III) nitrate nonahydrate ($Fe(NO_3)_3{\cdot}9\,H_2O$) precursors, followed by pre-pyrolysis and sintering. For substitution with calcium, we added calcium(II) nitrate hydrate ($Ca(NO_3)_2{\cdot}H_2O$) in suitable amounts to the precursor mixture. Figure 1a shows the x-ray diffraction (XRD) patterns of $Bi_{1-x}Ca_xFeO_{3-\delta}$ polycrystalline thin films (thickness: 200 nm) grown on fluorine-doped tin oxide (FTO) coated glass substrates where $x = 0, 0.05, 0.1, 0.2, 0.3$ describes the percentage of substitution with calcium. Pure $BiFeO_3$ thin films ($x = 0$) show a rhombohedrally distorted perovskite structure R3c (ICSD 8823) with one characteristic peak at $2\theta = 22.4°$ (012) as well as a double peak at $2\theta = 31.7°$ (104) and 32° (110), without any secondary crystalline phases present. For increasing calcium substitution ($x > 0.1$), the double peak merges into a single peak which shifts toward higher $2\theta$ angles. At $x = 0.3$, this peak emerges at $2\theta = 32.4°$ (200), which is indicative of the tetragonal $BiFeO_3$ phase I4/mcm (ICSD 165905). Quantitative phase analysis was performed by refining the scale factors of the individual crystalline phases. The Rietveld refinement results of all measurements are summarized in Table S1 (Supporting Information) and a representative refinement is shown in Figure S1. Figure 1b quantifies the phase composition of $Bi_{1-x}Ca_xFeO_{3-\delta}$ extracted from the XRD patterns in dependence of the calcium content $x$, showing a phase transition from R3c to I4/mcm for increasing x, with the major phase change occurring at $x = 0.2$. We attribute the change to lattice contraction and hence a decrease of the unit cell volume which may originate from the smaller ionic radius of calcium (100 pm) compared to the ionic radius of bismuth (117 pm). This agrees with an earlier study of Troyanchuk et al. who also observed this phase transition at $x = 0.2$ [23]. We note that, in Bragg-Brentano reflection mode, the reflections from the $BiFeO_3$ thin films are overlaid by the signature of the FTO/glass underneath which, for reference, is also shown in Figure 1a.

$$\frac{1-x}{2}Bi_2O_3 + xCaO + \frac{1}{2}Fe_2O_3 \rightleftharpoons (1-x)\,Bi_{Bi}^{\times} + xCa_{Bi}' + Fe_{Fe}^{\times} + \frac{x}{2}V_O^{\cdot\cdot} + \left(3-\frac{x}{2}\right)O_O^{\times} \quad (1)$$

$$\frac{1-x}{2}Bi_2O_3 + xCaO + \frac{1}{2}Fe_2O_3 + \frac{x}{4}O_2 \rightleftharpoons (1-x)\,Bi_{Bi}^{\times} + xCa_{Bi}' + Fe_{Fe}^{\times} + xh^{\cdot} + 3O_O^{\times} \quad (2)$$

The aliovalent substitution of $Bi^{3+}$ with $Ca^{2+}$ requires charge compensation as denoted in Equation 1 and 2 (Kröger-Vink notation) [24–26]. The substitution creates negative point charges which can be compensated by expulsion of oxygen, leading to oxygen vacancies [27]. According to equation 1, one oxygen vacancy can compensate two negative point charges and, thus, we expect an increasing number of oxygen vacancies toward stronger calcium substitution. This increase of oxygen vacancies can contribute to the unit cell volume reduction described above [28]. Yet, the negative point charges can also be compensated by the creation of positive free charge carriers (equation 2). This would result in a p-type semiconductor with enhanced hole conductivity. Indeed, the electrical conductivity of $Bi_{1-x}Ca_xFeO_{3-\delta}$ thin films enhances toward increasing calcium substitution $x$ as depicted in Figure 2a. For this measurement, we utilize the FTO-electrode underneath the $Bi_{1-x}Ca_xFeO_{3-\delta}$ and completed the MFM devices by thermal evaporation of silver (Ag) electrodes on top (Figure 2a, inset). In agreement with the literature [29, 30], the conductivity increases by four orders of magnitude, from $\sigma = (2.44 \pm 2.00) \times 10^{-11}$ S cm$^{-1}$ of pure $BiFeO_3$ to $\sigma = (2.83 \pm 0.98) \times 10^{-7}$ S cm$^{-1}$ at $x = 0.3$.

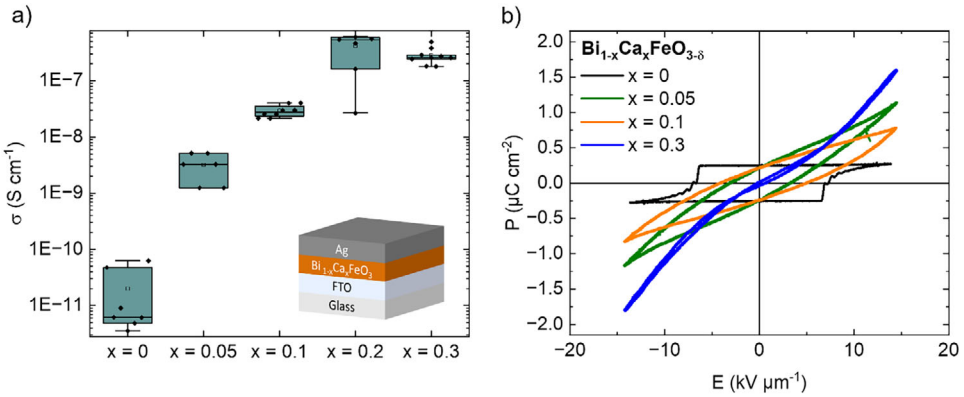


**FIGURE 2** | (a) Electrical conductivity $\sigma$ of $Bi_{1-x}Ca_xFeO_{3-\delta}$ thin films in MFM devices as a function of x. The conductivity improves by four orders of magnitude toward larger x. Inset: device architecture. (b) Ferroelectric hysteresis loops (polarization vs. electrical field, P-E) of $Bi_{1-x}Ca_xFeO_{3-\delta}$ thin films (x = 0, 0.05, 0.1, 0.3), measured at room temperature with a triangle waveform of the electric field at a frequency of 1 Hz.

## 3 | Ferroelectric Properties

Pure $BiFeO_3$ in its R3c phase is a known ferroelectric whereas the calcium-substituted $Bi_{1-x}Ca_xFeO_{3-\delta}$ in its I4/mcm phase (*i.e.* $x > 0.2$) does not exhibit ferroelectricity due to an inversion center of the centrosymmetric tetragonal structure. In order to study the ferroelectric properties of the $Bi_{1-x}Ca_xFeO_{3-\delta}$ series, we utilized the MFM devices described above. The ferroelectric polarization of $Bi_{1-x}Ca_xFeO_{3-\delta}$ thin films was measured in a Sawyer-Tower circuit at room temperature. The resulting polarization-electric field (*P-E*) hysteresis loops are depicted in Figure 2b. In pure $BiFeO_3$, we observed open hysteresis loops and a saturation of the polarization. The magnitude of the remnant polarization compares to previous studies using similar fabrication techniques [31–33]. The open hysteresis loop and thus the ferroelectric nature of the compounds are very well in agreement with the predominant R3c crystal phase, that was observed in the XRD analysis in Figure 1b. We found the same remnant polarizations at substitutions with calcium of $x = 0.05$ and $x = 0.1$, but the enhanced conductivity of the sample (Figure 2a) impeded saturation of the polarization, potentially amplified by the uncompensated Sawyer-Tower setup. To differentiate between the contributions from ferroelectric switching, ion migration and leakage currents, we performed frequency-dependent *P-E* hysteresis measurements in the range of 1 Hz – 1 kHz. Although we found some frequency dispersion in the *P-E* loops, which we attribute to ion migration and leakage currents, the observed hysteresis is dominated by ferroelectric switching (Figure S2). In contrast, at $x = 0.3$, no open hysteresis loop is detected, consistent with its nonferroelectric I4/mcm crystal structure. We note that, at $x = 0.2$, the *P-E* loop measurements did not yield any reproducible results, which indicates once again that $x = 0.2$ is very close to the ferroelectric-nonferroelectric transition. This result agrees with the mixed R3c and I4/mcm crystal structure shown in Figure 1b. It also agrees with reports by Troyanchuk et al. and Yang et al. who investigated the phase diagram of calcium-substituted $BiFeO_3$ and who concluded that the piezoelectric effect disappears at substitutions of $x > 0.2$ due to the formation of a centrosymmetric space group [23, 34]. Since ferroelectric materials are a subgroup of piezoelectric materials, their loss of piezoelectricity is in direct agreement with the suppression of the ferroelectric properties in this work.

## 4 | Photoresponse

To investigate how the ferroelectric polarization in $Bi_{1-x}Ca_xFeO_{3-\delta}$ influences the photoresponse of the corresponding MFM device, we again sandwiched the $Bi_{1-x}Ca_xFeO_{3-\delta}$ layers between FTO and Ag electrodes, both of which were deliberately chosen for their allegedly similar work function ($\Phi_{FTO} = 4.4$ eV [35], $\Phi_{Ag} = 4.33$ eV [36]). The relevant transport energies of the individual materials (before contact) are illustrated in Figure S3. We further chose $Bi_{1-x}Ca_xFeO_{3-\delta}$ compositions representative of both phases: $x = 0.1$ for the ferroelectric R3c phase and $x = 0.3$ for the nonferroelectric I4/mcm phase. Prior to the *J–V* sweeps, a DC poling voltage of 2 V was applied to set the polarization state (up, down) of the ferroelectric samples (for consistency, the nonferroelectric samples were subjected to the same "poling" process). The applied poling voltage was maintained until the polarization response saturated. The *J–V* curves were recorded using voltage sweep rates below 100 mV $s^{-1}$ to ensure quasi-static current responses.

### 4.1 | MFM Devices in the Dark

#### 4.1.1 | Nonferroelectric Devices

Figure 3a shows the dark current response (*J–V* curve) of the nonferroelectric sample ($x = 0.3$). In absence of ferroelectricity, the current-voltage characteristics can be described using the classical metal-semiconductor-metal (MSM) model, consisting of two opposing Schottky junctions at the metal-semiconductor interfaces. The corresponding simplified equivalent circuit is depicted in the inset of Figure 3a. Figure 3b illustrates the corresponding band diagram under bias voltage. The Schottky barrier height at each interface is determined by the difference of the work function of the metal electrode and the electrochemical potential of the semiconductor. In contact, the semiconductor is depleted close to the interface with the metal electrode, leaving behind immobile ionized acceptors. These acceptors create a built-in field that bends the bands and opposes further charge carrier diffusion [37]. Both electrodes (FTO, Ag) form barriers of almost identical heights and thus depletion regions of similar

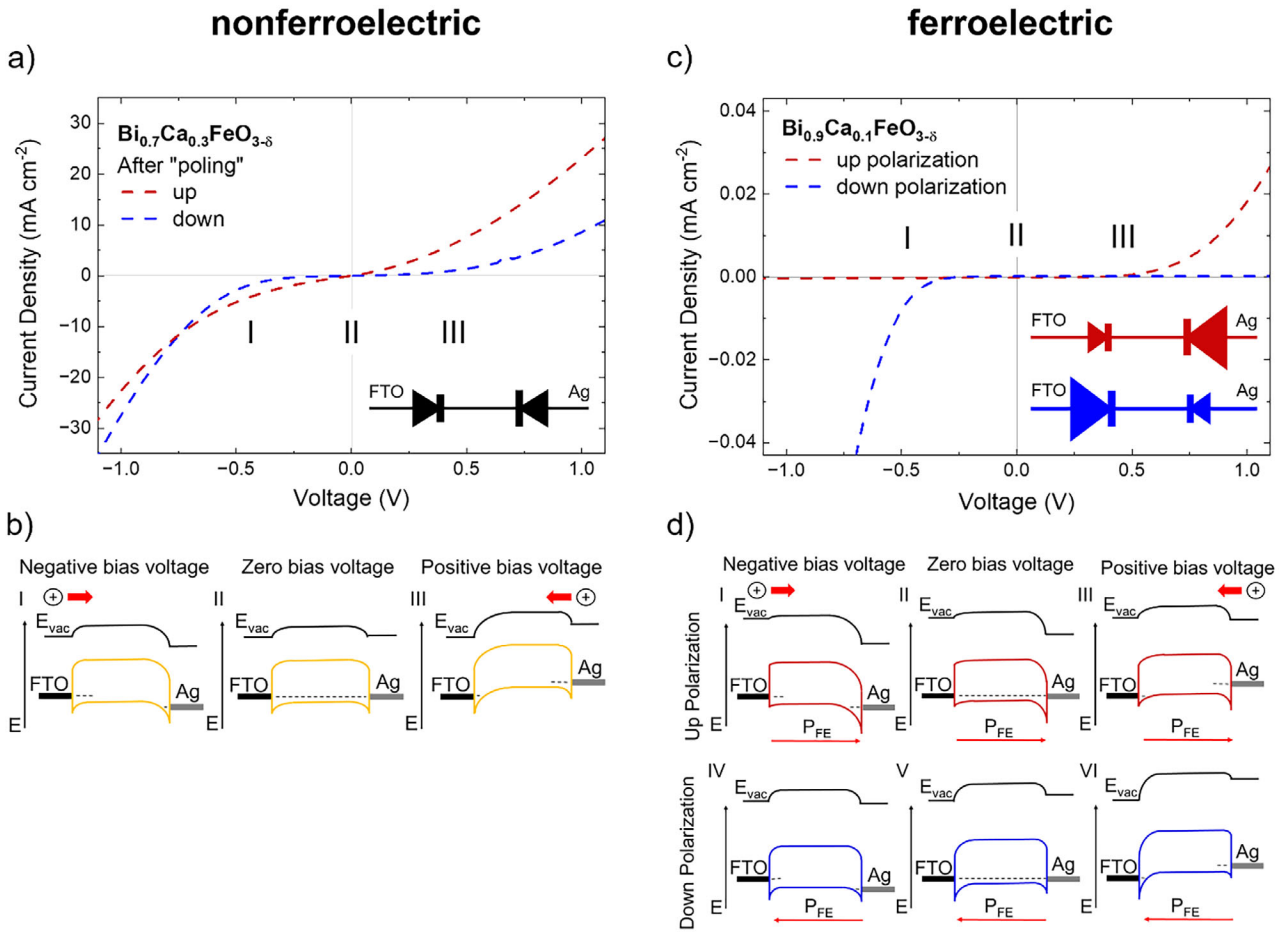


**FIGURE 3** | (a) *J–V* response of the nonferroelectric sample ($x = 0.3$) in the dark. The inset shows the simplified equivalent circuit of two opposing Schottky junctions. (b) Schematic band diagram with two Schottky junctions at the opposing electrode interfaces under bias voltage. The application of a bias voltage affects the width of their depletion region as illustrated in panels I, II, and III, representing negative bias voltage, zero bias voltage, and positive bias voltage, respectively. (c) *J–V* response of the ferroelectric sample ($x = 0.1$) in the dark. The inset shows the simplified equivalent circuit for the up and down polarization configuration, the sizes of the symbols represent the barrier heights. (d) Schematic band diagram with two Schottky junctions at the opposing electrode interfaces. In the up (down) polarization configuration, panels II (V) show the increased Schottky barrier height resulting from the accumulation of positive polarization charges under zero bias voltage. Panels I and III (IV and VI) illustrate how negative and positive bias voltages influence the width of the depletion region in the up (down) configuration.

widths, resulting in the almost symmetric band structure shown in Figure 3b (regime II). Under an external bias voltage, each depletion region adjusts to balance the applied field, expanding under reverse bias voltage or contracting under forward bias voltages. Because the device contains two opposite Schottky junctions, one of the two depletion regions expands while the other contracts, depending on the polarity of the applied voltage. The application of a positive bias voltage forward-biases the Schottky junction at the Ag electrode, reducing its depletion width and enabling current injection through this interface. At the same time, the opposite junction at the FTO electrode becomes reverse-biased, increasing its depletion width and thus limiting the device current. The corresponding modification of the band diagram is illustrated in Figure 3b (regime III). Conversely, the application of a negative bias voltage inverts the roles of the two junctions, but effectively produces the same *J–V* behavior. The respective band diagram under negative bias voltage is depicted in Figure 3b (regime I). Yet, the small asymmetry of the electrode work functions results in slightly different magnitudes of the barrier height and thus the device current.

We noted a minor difference in the *J–V* curves depending on the "poling" direction, up or down. In absence of ferroelectricity, we attribute this difference to minor ion migration (oxygen vacancies) and its influence on the electronic interface states at the metal-semiconductor contact [38, 39].

### 4.1.2 | Ferroelectric Devices

In contrast, the ferroelectric sample ($x = 0.1$) produces a polarization dependent asymmetry in the *J–V* curves, Figure 3c (in the dark). While the nonferroelectric MSM device can be modeled using two opposing Schottky junctions, the ferroelectric MFM device requires accounting of the effect of ferroelectric polarization on the Schottky junctions:

In the up-polarization configuration, positive bound polarization charges accumulate at the interface to the Ag electrode, adding to the negative space charges within the depletion region. This results in a larger (dominant) Schottky barrier height and

wider depletion region. At the opposing Schottky junction, at the FTO interface, the barrier height and the width of the depletion region is reduced due to the accumulation of negative polarization charges [17]. This leads to the equivalent circuit for the up-polarization configuration depicted in red in the inset of Figure 3c. The corresponding modification of the band structure is illustrated in Figure 3d (regime II). This up-polarization induced asymmetry results in an increased Schottky barrier height at the Ag electrode, which in turn results in an increased forward voltage under positive bias voltage, Figure 3d (regime III). Under negative bias voltages, Figure 3d (regime I), the enhanced Schottky junction at the Ag interface is reverse-biased and blocks the device current.

In the down-polarization configuration, the enhanced Schottky junction is located at the FTO interface and the reduced Schottky junction at the Ag interface, effectively inverting the device and the *J*–*V* curve. The corresponding band diagrams are shown in Figure 3b (IV, V, VI). Because of the principal minor difference in work function of the electrodes, we observed differences in forward voltages and absolute current densities.

We note that the lower conductivity of the ferroelectric sample leads to a much lower overall current density at a given bias compared to the non-ferroelectric sample.

### 4.2 | MFM Devices Under Illumination

The implementation of MFM architectures into solar cells in the past has prompted us to investigate the interplay of the opposing Schottky barriers under illumination. For this purpose, we characterized the devices by recording *J*–*V* curves under illumination ($\lambda$ = 400 nm) through the glass substrate and the transparent FTO electrode. We note that calcium substitution has only a minor influence on the absorption of the $Bi_{1-x}Ca_xFeO_{3-\delta}$ thin films and hence their band gap (Figure S4).

#### 4.2.1 | Nonferroelectric Devices

The *J*–*V* curves of the nonferroelectric samples in Figure 4a are point symmetric and effectively show no photocurrent, independent of the direction of previously applied voltage ("poling"). The most notable effect was a minor change in the slope of the *J*–*V* curves compared to the dark *J*–*V* curves which we attribute to some photoconductivity of $BiFeO_3$ as reported earlier [40]. The symmetry of the *J*–*V* curves of the nonferroelectric device hints at a lack in directionality and separation of the photo-generated charge carriers which agrees well with the previously discussed symmetric band diagram in Figure 3b (regime II).

#### 4.2.2 | Ferroelectric Devices

In stark contrast, the ferroelectric device exhibits a pronounced polarization-dependent photocurrent response.

In the up-polarization configuration, Figure 4b, the ferroelectric device shows a typical solar cell photocurrent response: the *J*–*V* curve resembles the shape of a photodiode with a photovoltage of $V$ = +594 mV at $J$ = 0 mA cm$^{-2}$ which is a remarkable potential difference when two electrodes with similar work functions are used and clearly shows the effect of the ferroelectric polarization on the photoresponse. The photocurrent was $J$ = -974 μA cm$^{-2}$ at $V$ = 0 V.

In the down polarization configuration, Figure 4c, we found an inverted photocurrent response, with a negative photovoltage of $V$ = -210 mV at $J$ = 0 mA cm$^{-2}$ and a positive photocurrent of $J$ = +6.3 μA cm$^{-2}$ at $V$ = 0 V.

In Schottky junctions, the built-in electric field within the depletion region drives electrons and holes in opposite directions, enabling separation and collection of the photogenerated charge carriers. If the sample exhibits a net ferroelectric polarization, the interface between the metal and the ferroelectric is modified, and so is the Schottky barrier height and its adjacent depletion region. Under illumination, the built-in field drives the photocurrent against the polarization direction. For zero applied bias voltage ($V$ = 0 V) the resulting asymmetry in Schottky barrier heights and depletion widths directly determines the magnitude and direction of the photocurrent. As in the dark case, the overall current under illumination remains limited by the reverse-biased junction. The absolute difference in photocurrent between the up- and down-polarization configuration may also arise from the distinct properties of the two electrodes. Ag is an ideal metal with an effectively infinite density of screening charges, producing a depletion zone that extends far into the ferroelectric layer. In contrast, FTO possesses a lower concentration of free-electrons, approximately seven orders of magnitude lower, causing a portion of the depletion region to extend into the electrode [41]. This reduces the width of the depletion region within the ferroelectric layer, which in turn results in a smaller photocurrent response when the FTO side acts as the dominant junction.

We note that ion migration may produce similar *J*–*V* hysteresis and thus can be misinterpreted as a ferroelectric response. Yet, a *J*–*V* hysteresis is only produced by the ferroelectric device with lower calcium substitution and hence an allegedly lower density of oxygen vacancies, i.e. ions (Figure 4a,b). Thus, we conclude that ion migration plays only a minor role for the effects observed in the MFM device here.

## 5 | Conclusion

In this study, we explored the effect of ferroelectricity on the photoresponse of MFM devices. The devices are governed by two opposite Schottky junctions at the interfaces to the electrodes. With two electrodes of similar work function, the electronic structure and the electronic response of nonferroelectric devices in the dark and under illumination are symmetric. Directionality can be introduced by ferroelectric polarization which enhances or reduces both the barrier height and the width of the depletion region. These findings provide criteria for future MFM device optimization: to enhance the performance of solar cells comprising semiconducting ferroelectrics for light harvesting, such as $Bi_{1-x}Ca_xFeO_{3-\delta}$, tailoring both the barrier height and the width of the depletion region by ferroelectric polarization will be essential. Ideally, the reverse Schottky junction will be eliminated to not

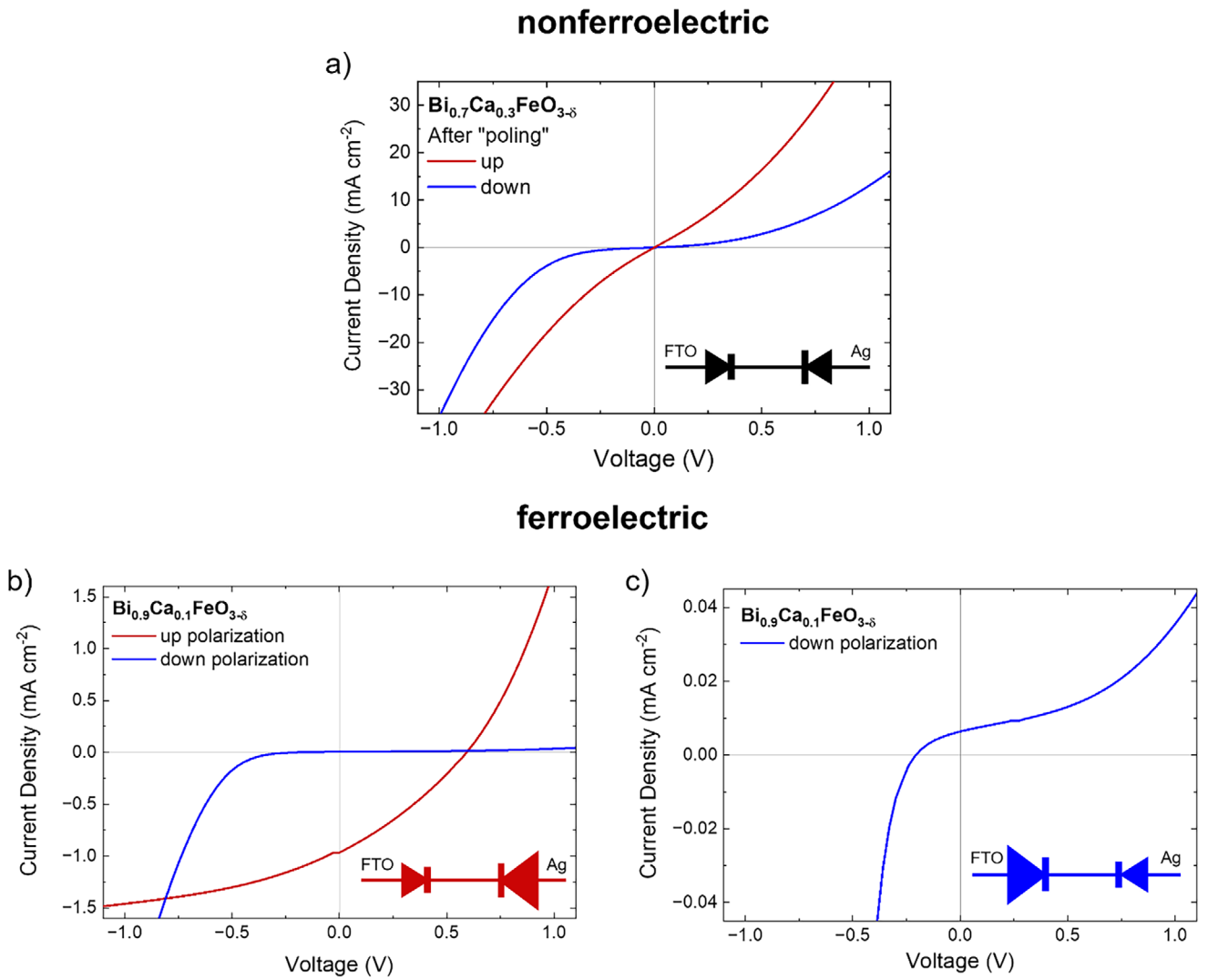


**FIGURE 4** | (a) The *J–V* curve of the nonferroelectric sample (x = 0.3) under illumination ($\lambda$ = 400 nm) exhibits no photocurrent and no directionality regardless of the previously applied "poling" voltage. The simplified equivalent circuit is displayed in the inset. (b) In contrast, the ferroelectric sample (x = 0.1) exhibits directionality induced by the ferroelectric polarization. Its photovoltaic response depends on the polarization direction. (c) Magnified J–V response of the ferroelectric sample in the down-polarization configuration.

hinder the injection of charge carriers (in the dark) or the extraction of charge carriers (under illumination).

## 6 | Experimental Section/Methods

### 6.1 | Sol Preparation

The precursors bismuth(III) nitrate pentahydrate ($Bi(NO_3)_3{\cdot}5\ H_2O$, 98%, Sigma-Aldrich) and iron(III) nitrate nonahydrate ($Fe(NO_3)_3{\cdot}9\ H_2O$, 98%, Merck) were used to synthesize $BiFeO_3$. For calcium substituted $BiFeO_3$, calcium(II) nitrate hydrate ($Ca(NO_3)_2{\cdot}H_2O$, 99.995%, Thermo Fisher Scientific) was used to partially replace bismuth according to the nominal $Bi_{1-x}Ca_xFeO_{3-\delta}$ composition. A saturated $Fe(NO_3)_3$ solution (1.5 g $mL^{-1}$) was prepared in deionized water and stirred (50°C, 2 min). $Bi(NO_3)_3$ was dissolved in citric acid ($C_6H_8O_7$, Merck, 1 M, 1.4 g $mL^{-1}$) and stirred (50°C, 2 min). The iron nitrate solution was then added to the bismuth nitrate solution and stirred until fully mixed (at least 5 min). The resulting sol was aged overnight before further processing.

### 6.2 | Fabrication of $Bi_{1-x}Ca_xFeO_{3-\delta}$ Thin-Films and Devices

Fluorine doped tin oxide (FTO) coated glass substrates (TCO-13-15, Solaronix) were laser-patterned and cleaned sequentially in ultrasonic baths of acetone and isopropanol (10 min each), followed by drying in a flow of nitrogen. To improve sol wetting, the FTO surface was treated with oxygen plasma (200 W, 0.6 mbar, 2.5 min, Atto system Diener Electronics). The $Bi_{1-x}Ca_xFeO_{3-\delta}$ sol was spin-coated (3000 rpm, 60 s, 60 µL), dried, and subjected to pre-pyrolysis on a hotplate (320°C, 3 K·$min^{-1}$, 30 min hold time every 30°C), followed by sintering in a muffle furnace (500°C, 3 K $min^{-1}$, 270 min hold time). The $Bi_{1-x}Ca_xFeO_{3-\delta}$ layer was applied in two coating cycles, yielding 200 nm ± 20 nm thick films. The film thickness was determined using a stylus profiler (Bruker,

DektakXT) Finally, silver electrodes were thermally evaporated ($10^{-6}$ mbar base pressure, 10 nm at 1 Å $s^{-1}$, 90 nm at 2–2.5 Å $s^{-1}$) to complete the device. The overlap of both electrodes yielded a photoactive area of 0.105 $cm^2$.

## 6.3 | Characterization

X-ray diffraction experiments were conducted at room temperature in Bragg-Brentano geometry using Cu K$\alpha$ radiation (Diffraction angles $2\theta$ = 5° to 95°, step size = 0.01°, Bruker D8 Advance diffractometer). The crystallographic database entries for $BiFeO_3$ were retrieved from the inorganic crystal structure database (ICSD) (https://icsd.products.fiz-karlsruhe.de/, FIZ Karlsruhe—Leibnitz Institute for Information Infrastructure) with the ICSD collection code 8823 (R3c—$BiFeO_3$) and 165905 (I4/mcm—($Bi_{1-x}Ca_xFeO_{3-\delta}$). Phase quantity analysis was performed by Rietveld refinement of scaling factors using Profex/BGMN software (Version 5.2.9) [42].

A Sawyer-Tower circuit was employed to measure polarization-electric field (*P-E*) hysteresis loops at room temperature. The setup consisted of a function generator, a reference capacitor, and an oscilloscope. A triangular voltage signal (1 Hz, 6 $V_{pp}$) was applied across the sample using a function generator. The sample was connected in series with a known reference capacitance (0.1 µF), forming a voltage divider. The voltage across the reference capacitor, which is proportional to the charge displacement in the sample, was monitored using one channel of the oscilloscope. Simultaneously, the voltage across the sample was measured using a second channel. The two channels of the oscilloscope produced the XY coordinates of the resulting *P-E* plot, where the horizontal axis represents the voltage across the sample (proportional to the electric field), and the vertical axis represents the voltage across the reference capacitor (proportional to polarization).

*J–V* curves were recorded in dark and under UV-irradiation ($\lambda$ = 400 nm, 100 mW $cm^{-2}$, DELOLUX 20 / 400 Lamp, DELO-UNIPRO Light) with a source meter unit (Keithley 2400). Further information on the spectral output of the UV lamp and the intensity calibration are provided in Figure S5. Electrical conductivities $\sigma$ were obtained from the slope of the ohmic regime of the *J–V* curves, using the linear fit.


### Acknowledgments

We thank Rainer Nast for the laser-structuring of FTO substrates. All authors received funding by the Carl Zeiss foundation within the project KeraSolar. A.C. and H.R. acknowledge further support by the Helmholtz program "Materials and Devices for the Energy Transition" (MTET).

Open access funding enabled and organized by Projekt DEAL.


### Conflicts of Interest

The authors declare no conflicts of interest.

### Data Availability Statement

The data that support the findings of this study are available from the corresponding author upon reasonable request.

### References


1. W. Ke and M. G. Kanatzidis, "Prospects for Low-Toxicity Lead-Free Perovskite Solar Cells," *Nature Communications* 10 (2019): 965, https://doi.org/10.1038/s41467-019-08918-3.

2. B. Saparov, "Next Generation Thin-Film Solar Absorbers Based on Chalcogenides," *Chemical Reviews* 122 (2022): 10575–10577, https://doi.org/10.1021/acs.chemrev.2c00346.

3. C. Paillard, X. Bai, I. C. Infante, et al., "Photovoltaics With Ferroelectrics: Current Status and Beyond," *Advanced Materials* 28 (2016): 5153–5168, https://doi.org/10.1002/adma.201505215.

4. W.-J. Yin, B. Weng, J. Ge, Q. Sun, Z. Li, and Y. Yan, "Oxide Perovskites, Double Perovskites and Derivatives for Electrocatalysis, Photocatalysis, and Photovoltaics," *Energy & Environmental Science* 12 (2019): 442–462, https://doi.org/10.1039/C8EE01574K.

5. L. Pintilie, I. Vrejoiu, G. Le Rhun, and M. Alexe, "Short-circuit Photocurrent in Epitaxial Lead Zirconate-titanate Thin Films," *Journal of Applied Physics* 101 (2007): 064109, https://doi.org/10.1063/1.2560217.

6. T. Choi, S. Lee, Y. J. Choi, V. Kiryukhin, and S.-W. Cheong, "Switchable Ferroelectric Diode and Photovoltaic Effect in $BiFeO_3$," *Science* 324 (2009): 63–66, https://doi.org/10.1126/science.1168636.

7. J. Zhang, X. Su, M. Shen, et al., "Enlarging Photovoltaic Effect: Combination of Classic Photoelectric and Ferroelectric Photovoltaic Effects," *Scientific Reports* 3 (2013): 2109, https://doi.org/10.1038/srep02109.

8. H. T. Yi, T. Choi, S. G. Choi, Y. S. Oh, and S.-W. Cheong, "Mechanism of the Switchable Photovoltaic Effect in Ferroelectric BiFeO3," *Advanced Materials* 23 (2011): 3403–3407, https://doi.org/10.1002/adma.201100805.

9. C. S. Tu, C.-M. Hung, Z.-R. Xu, et al., "Calcium-doping Effects on Photovoltaic Response and Structure in Multiferroic $BiFeO_3$ Ceramics," *Journal of Applied Physics* 114 (2013): 124105, https://doi.org/10.1063/1.4823856.

10. V. M. Fridkin, *Photoferroelectrics* (Springer, 1979).

11. Z. Dai and A. M. Rappe, "Recent Progress in the Theory of Bulk Photovoltaic Effect," *Chemical Physics Reviews* 4 (2023): 011303, https://doi.org/10.1063/5.0101513.

12. M.-M. Yang, A. Bhatnagar, Z.-D. Luo, and M. Alexe, "Enhancement of Local Photovoltaic Current at Ferroelectric Domain Walls in $BiFeO_3$," *Scientific Reports* 7 (2017): 43070, https://doi.org/10.1038/srep43070.

13. L. You, F. Zheng, L. Fang, et al., "Enhancing Ferroelectric Photovoltaic Effect by Polar Order Engineering," *Science Advances* 4 (2018): 3438, https://doi.org/10.1126/sciadv.aat3438.

14. J. Seidel, D. Fu, S.-Y. Yang, et al., "Efficient Photovoltaic Current Generation at Ferroelectric Domain Walls," *Physical Review Letters* 107 (2011): 126805, https://doi.org/10.1103/PhysRevLett.107.126805.

15. M. Qin, K. Yao, and Y. C. Liang, "High Efficient Photovoltaics in Nanoscaled Ferroelectric Thin Films," *Applied Physics Letters* 93 (2008): 122904, https://doi.org/10.1063/1.2990754.

16. P. W. M. Blom, R. M. Wolf, J. F. M. Cillessen, and M. P. C. M. Krijn, "Ferroelectric Schottky Diode," *Physical Review Letters* 73 (1994): 2107–2110, https://doi.org/10.1103/PhysRevLett.73.2107.

17. L. Pintilie and M. Alexe, "Metal-ferroelectric-metal Heterostructures With Schottky Contacts. I. Influence of the Ferroelectric Properties," *Journal of Applied Physics* 98 (2005): 124103, https://doi.org/10.1063/1.2148622.

18. G.-L. Yuan and J. Wang, "Evidences for the Depletion Region Induced by the Polarization of Ferroelectric Semiconductors," *Applied Physics Letters* 95 (2009): 252904, https://doi.org/10.1063/1.3268783.

19. J. Dho, X. Qi, H. Kim, J. L. MacManus-Driscoll, and M. G. Blamire, "Large Electric Polarization and Exchange Bias in Multiferroic $BiFeO_3$," *Advanced Materials* 18 (2006): 1445–1448, https://doi.org/10.1002/adma.200502622.

20. D. Sando, C. Carrétéro, M. N. Grisolia, A. Barthélémy, V. Nagarajan, and M. Bibes, "Revisiting the Optical Band Gap in Epitaxial BiFeO3 Thin Films," *Advanced Optical Materials* 6 (2018): 1700836, https://doi.org/10.1002/adom.201700836.

21. W. A. Wani, H. Venkataraman, and K. Ramaswamy, "Connecting Electrical Current Conduction and Urbach Energy in Doped $BiFeO_3$ Thin-films," *Materials Chemistry and Physics* 298 (2023): 127468, https://doi.org/10.1016/j.matchemphys.2023.127468.

22. H. K. Meena, K. Meena, R. Verma, et al., "Tuning of Optical Properties via Annealing of Bismuth Ferrite (BiFeO<sub>3</sub>) Thin Films," *Open Journal of Composite Materials* 14 (2024): 124–131, https://doi.org/10.4236/ojcm.2024.143009.

23. I. O. Troyanchuk, D. V. Karpinsky, M. V. Bushinskii, et al., "Crystal Structure and Properties of $Bi_{1-X}Ca_XFeO_3$ and $Bi_{1-X}Ca_XFeO_{1-X}Ti_XO_3$ Solid Solutions," *Journal of Experimental and Theoretical Physics* 107 (2008): 83–89, https://doi.org/10.1134/S106377610807008X.

24. X. Wang, S. Y. Wang, W. F. Liu, et al., "Novel Electrical Conductivity Properties in Ca-doped $BiFeO_3$ Nanoparticles," *Journal of Nanoparticle Research* 17 (2015): 209, https://doi.org/10.1007/s11051-015-3018-1.

25. W. Mao, Q. Yao, N. Liu, et al., "Effect of Ca Doping on Photovoltaic Effect of $BiFeO_3$," *Applied Physics A* 127 (2021): 508, https://doi.org/10.1007/s00339-021-04651-1.

26. M. Schrade, N. Masó, A. Perejón, L. A. Pérez-Maqueda, and A. R. West, "Defect Chemistry and Electrical Properties of $BiFeO_3$," *Journal of Materials Chemistry C* 5 (2017): 10077–10086, https://doi.org/10.1039/C7TC03345A.

27. T. Zhang, W. Zhao, Q. Wu, et al., "Oxygen Vacancy Induced Electrical Conductivity Enhancement in Ca-Doped $BiFeO_3$ Thin Films," *Journal of Alloys and Compounds* 1008 (2024): 176826, https://doi.org/10.1016/j.jallcom.2024.176826.

28. R. Wang, H. Shu, W. Mao, et al., "Study on the Magnetic and Ferroelectric Properties of Ca-Doped and (Eu, Ca)Co-Doped $BiFeO_3$," *Journal of Superconductivity and Novel Magnetism* 30 (2017): 999–1002, https://doi.org/10.1007/s10948-016-3883-6.

29. T. Zhang, W. Zhao, Q. Wu, et al., "Oxygen Vacancy Induced Electrical Conductivity Enhancement in Ca-doped $BiFeO_3$ Thin Films," *Journal of Alloys and Compounds* 1008 (2024): 176826, https://doi.org/10.1016/j.jallcom.2024.176826.

30. S. Nandy, K. Kaur, P. S. V. Mocherla, B. R. K. Nanda, and C. Sudakar, "Oxygen Vacancy Induced Photoconductivity Enhancement in Bi1-xCaxFeO$_{3-\delta}$ Nanoparticle Ceramics: A Combined Experimental and Theoretical Study," *Journal of Applied Physics* 124 (2018): 195108, https://doi.org/10.1063/1.5055742.

31. T. Lei, W. Cai, C. Fu, et al., "The Effects of Grain Size on Electrical Properties and Domain Structure of $BiFeO_3$ Thin Films by Sol–Gel Method," *Journal of Materials Science: Materials in Electronics* 26 (2015): 9495–9506, https://doi.org/10.1007/s10854-015-3690-z.

32. H. Liu, Z. Liu, Q. Liu, and K. Yao, "Ferroelectric Properties of $BiFeO_3$ Films Grown by Sol–Gel Process," *Thin Solid Films* 500 (2006): 105–109, https://doi.org/10.1016/j.tsf.2005.11.041.

33. Y. Wang, Q.-H. Jiang, H.-C. He, and C.-W. Nan, "Multiferroic $BiFeO_3$ Thin Films Prepared via a Simple Sol-Gel Method," *Applied Physics Letters* 88 (2006): 142503, https://doi.org/10.1063/1.2191947.

34. C.-H. Yang, J. Seidel, S. Y. Kim, et al., "Electric Modulation of Conduction in Multiferroic Ca-doped $BiFeO_3$ Films," *Nature Materials* 8 (2009): 485–493, https://doi.org/10.1038/nmat2432.

35. A. Andersson, N. Johansson, P. Bröms, et al., "Fluorine Tin Oxide as an Alternative to Indium Tin Oxide in Polymer LEDs," *Advanced Materials* 10 (1998): 859–863, https://doi.org/10.1002/(SICI)1521-4095(199808)10:11%3C859::AID-ADMA859%3E3.0.CO;2-1.

36. E. W. J. Mitchell and J. W. Mitchell, "The Work Functions of Copper, Silver and Aluminium," *Proceedings of the Royal Society of London Series A* 210 (1951): 70–84.

37. E. H. Rhoderick, *Metal-Semiconductor Contacts* (Clarendon Pr, 1978).

38. J. S. Lim, J. H. Lee, H.-S. Park, et al., "Ultrafast Collective Oxygen-Vacancy Flow in Ca-Doped $BiFeO_3$," *NPG Asia Materials* 10 (2018): 943–955, https://doi.org/10.1038/s41427-018-0087-5.

39. N. Du, N. Manjunath, Y. Li, et al., "Field-Driven Hopping Transport of Oxygen Vacancies in Memristive Oxide Switches With Interface-Mediated Resistive Switching," *Physical Review Applied* 10 (2018): 054025, https://doi.org/10.1103/PhysRevApplied.10.054025.

40. S. R. Basu, L. W. Martin, Y. H. Chu, et al., "Photoconductivity in $BiFeO_3$ Thin Films," *Applied Physics Letters* 92 (2008): 091905, https://doi.org/10.1063/1.2887908.

41. M. Qin, K. Yao, and Y. C. Liang, "Photovoltaic Mechanisms in Ferroelectric Thin Films With the Effects of the Electrodes and Interfaces," *Applied Physics Letters* 95 (2009): 022912, https://doi.org/10.1063/1.3182824.

42. N. Doebelin and R. Kleeberg, "Profex: A Graphical User Interface for the Rietveld Refinement Program BGMN," *Journal of Applied Crystallography* 48 (2015): 1573–1580, https://doi.org/10.1107/S1600576715014685.

## Supporting Information

Additional supporting information can be found online in the Supporting Information section.

**Supporting File:** apxr70166-sup-0001-SuppMat.pdf.